RSC Applied Interfaces

Accepted Manuscript

This article can be cited before page numbers have been issued, to do this please use: B. A. Sadeghi, C. Wölke, M. Shevchuk, J. Minar, S. Krämer, M. C. Stan, M. Weiling, M. Baghernejad, S. Nowak, G. Röschenthaler, M. Grünebaum, M. Winter and I. Cekic-Laskovic, *RSC Appl. Interfaces*, 2025, DOI: 10.1039/D5LF00138B.

ROYAL SOCIETY OF CHEMISTRY

rsc.li/RSCApplInter

View Article Online
DOI: 10.1039/D5LF00138B

ARTICLE

Impact of Phosphazene-based Compounds in an Electrolyte Additive Mixture for Enhanced Safety and Performance of NMC811||Si-Graphite Cell Chemistry

Received 00th January 20xx,
Accepted 00th January 20xx

DOI: 10.1039/x0xx00000x

Bahareh Alsadat Sadeghi,[a] Christian Wölke,[a] Mykhailo Shevchuk,[a] Marian Stan,[a] Jaroslav Minar,[b] Matthias Weiling,[a] Susanna Krämer,[a] Masoud Baghernejad,[a] Sascha Nowak,[b] Gerd-Volker Röschenthaler,[c] Mariano Grünebaum,[a] Martin Winter,[a,b] Isidora Cekic-Laskovic[a*]

Addressing the critical need for enhanced safety and performance in lithium-ion batteries (LIBs), this work presents a comprehensive evaluation of a novel flame-retardant electrolyte additive, 2,2,2-trifluoroethoxy(pentafluoro)cyclo-triphosphazene (CF_3PFPN), in combination with vinylene carbonate (VC) and 2-phenoxy-1,3,2-dioxaphospholane (PhEPi) for high-energy NMC811||Si-graphite (20 % Si) cells. This synergistic additive mixture not only demonstrates superior flame-retardant properties compared to a non-fluorinated analogue but also yields improvements in discharge capacity. Detailed investigation of the solid electrolyte interphase (SEI) and cathode electrolyte interphase (CEI) formation reveals the beneficial contributions of each component, leading to reduced interfacial resistance and enhanced electrochemical performance. Furthermore, gas chromatography-mass spectrometry (GC-MS) analysis confirms the effective suppression of electrolyte degradation. These findings highlight the substantial potential of tailored electrolyte additive combinations, particularly incorporating fluorinated phosphazenes, to simultaneously advance the safety and energy density of LIBs utilizing silicon-based anodes.

Introduction

Lithium ion batteries (LIBs), known for their high energy density, and rechargeable nature have become a fundamental element of modern portable electronics, electric vehicles and stationary energy storage systems[1,2]. In spite of notable advancements in improving the relevant electrochemical properties, safety concerns still remain unsolved[3]. The primary safety challenges in LIBs stem from the intrinsic properties of the used materials and operating conditions, which include highly reactive electrode materials and flammable organic electrolyte solvents. The presence of the often volatile and flammable components in the electrolyte leads to increased susceptibility of a cell to failure under abusive operating conditions, such as overcharging, external impacts or heat shocks. Under these conditions, LIBs can experience thermal runaway; a chain reaction of exothermic events that can rapidly escalate temperatures and cause catastrophic failure such as explosion and release of toxic gases[4].

In general, to enhance LIB safety, the development of non-flammable electrolyte formulations is required. Incorporating flame-retardant additives (FRAs), such as phosphorus-based compounds[5–8] e.g., phosphazenes[9–11], and halogen-based compounds[12], into the electrolytes, suppress combustion or delay fire spread[8,12]. Cyclic phosphazenes are a well-known class of organophosphorus FRAs that effectively balance flame retardancy and electrochemical performance of the resulting cell chemistry[13]. Phosphazenes are generally classified into cyclic phosphorus-nitrogen and linear phosphorus-nitrogen compounds (**Figure 1a** and **1b**). Cyclic phosphazenes are inherently non-flammable and can be polymerized to form larger phosphazene structures.[14–16] Prakash and co-workers reported the first application of hexamethoxycyclophosphazene (HMPN) as a flame retardant additive in LIBs, demonstrating its effectiveness without compromising the cell performance[17]. Since achieving a balance between flame retardancy and interfacial properties is crucial, a successful strategy to further enhance the efficiency of cyclophosphazenes is related to incorporation of fluorine to address both flame retardancy and electrochemical compatibility. Recent studies have revealed that fluorinated cyclophosphazenes such as ethoxy(pentafluoro)cyclotriphosphazene (PFPN, **Figure 1c**), exhibit dual functionality[18,19]: they act as efficient FRA by forming P and N radicals to terminate combustion reactions, and the generated F radicals during thermal decomposition, capture

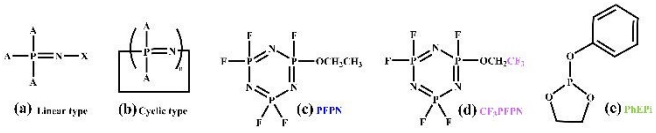

Figure 1. (a, b) Representative structures of phosphazenes, (c) ethoxy(pentafluoro)cyclotriphosphazene (PFPN), (d) 2,2,2- trifluoro-ethoxy-pentafluorocyclotriphosphazene (CF_3PFPN) and (e) 2-phenoxy-1,3,2-dioxaphospholane (PhEPi).

[a] Helmholtz-Institute Münster, IMD-4, Forschungszentrum Jülich GmbH, Corrensstraße 48, 48149 Münster, Germany, E-mail: i.cekic-laskovic@fz-juelich.de.
[b] University of Münster, MEET Battery Research Center, Corrensstraße 46, 48149 Münster, Germany
[c] Constructor University Bremen GmbH, School of Science, Campus Ring 1, Bremen 28759, Germany
† Supplementary Information (SI) available: See DOI: 10.1039/x0xx00000x

H radicals generated during electrolyte combustion, effectively terminating the combustion reaction[12,14,19–22]. Additionally, these additives contribute to forming an effective solid electrolyte interphase (SEI) particularly in cells with Si-based anodes [23–25].

Based on these findings, the structure of PFPN (**Figure 1c**) was further modified to fully leverage the advantages of fluorination. Therefore, as shown in **Figure 1c**, the methyl group in PFPN was substituted by a trifluoromethyl group resulting in the 2,2,2-trifluoroethoxy-pentafluorocyclotriphosphazene (CF_3PFPN), **Figure 1d.**

In recent work, it was demonstrated that the performance of NMC811||Si-graphite (Si-Gr) cell chemistry, where the anode contained 20 % Si, was considerably improved in presence of the optimized additive/co-solvent mixture[26], containing 2-phenoxy-1,3,2-dioxaphospholane (PhEPi) (**Figure 1e**) and vinylene carbonate (VC). Herein, the focus is set on the synthesized FRA, CF_3PFPN, and its synergistic impact with VC and PhEPi on the electrochemical performance and increased safety of the resulting NMC811‖Si-Gr cell chemistry.

Experimental Part

2.1. Synthesis of CF3PFPN and product characterization

In a two-neck 250 mL round-bottom flask, Na_2CO_3 (4.3 g, 40.8 mmol, 1.2 eq) was flame-dried for 5 min under vacuum. After cooling to room temperature (RT), the flask was charged with Ph_2O (135 mL) followed by a solution of $P_3N_3F_6$ (12.6 g, 51 mmol, 1.5 eq) in 15 mL of triglyme. Then CF_3CH_2OH› (1.79 g, 17.9 mmol, 0.52 eq) was added, and the resulting mixture was stirred for 24 h at RT. The second portion of CF_3CH_2OH (0.80 g, 8 mmol, 0.24 eq) was added, and stirring was continued overnight. The third portion of CF_3CH_2OH (0.43 g, 4.3 mmol, 0.13 eq) was added, and stirring was continued for 24 h. The fourth portion of CF_3CH_2OH (0.25 g, 2.5 mmol, 0.07 eq) was added, and stirring was continued for 8 h. The last portion of CF_3CH_2OH (0.13 g, 1.3 mmol, 0.04 eq) was added, and stirring was continued overnight. Thus, a total of 3.4 g (34 mmol, 1.00 eq) of trifluoroethanol were used in the reaction. Volatiles were carefully distilled into a liquid nitrogen trap under a vacuum. The remaining liquid was distilled at ambient pressure. Fraction boiling at 96–106 °C contained the title compound (yield 7.1 g, 63 %). The synthesis route is illustrated in Scheme 1.

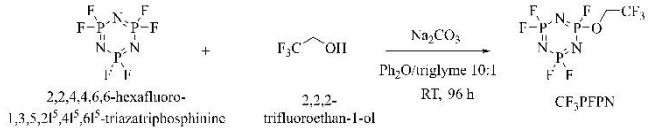

Scheme 1: Synthesis route of the CF_3PFPN

The purity of the sample from the NMR spectra alone is determined to be ≥ 98 % (**Figure S13** and **S14**)

^{1}H NMR (400 MHz, $CDCl_3$): δ = 4.45 (dq, *J* = 10.4, 7.6 Hz) ppm.

^{19}F NMR (376 MHz, $CDCl_3$): δ = –64.1 (dm, 892.8 Hz, 1H), –68.7 (dm, 895.3 Hz, 4H), –75.0 (t, 7.5 Hz) ppm.

2.2. Electrode materials and electrolyte components

NMC811 single-sided electrode sheets with areal capacity of 1.67 mAh cm^{-2} and Si-Gr single-sided electrode sheets with 2 mAh cm^{-2}, containing 20% silicon, purchased from Targray, were kept in the dry room (dew point < 60 °C). They were punched in 14 mm and 15 mm diameter pieces for NMC811 and Si-Gr electrodes, respectively, and dried for 12 h at 120 °C under vacuum (10^{-2}-10^{-3} mbar) before use. Thereafter, they were stored in the argon-filled glovebox (MBraun Labmaster, H_2O and O_2 content <0.5 ppm). Li metal (500 µm thickness, purchased from China Energy Lithium CO. Ltd) was kept inside the argon-filled glovebox as well. Celgard 2500 as a separator for 2032-type coin cells were punched in 16 mm diameter, and Whatman grade GF/D were punched in 10, 13 mm diameter as a separator for Swagelok T-cells were dried overnight at 60 °C and stored in the argon-filled glovebox. All considered electrolyte components (EC, EMC, PFPN, CF_3PFPN, and $LiPF_6$) in battery grade were provided by Solvionic Co. VC was purchased from E–Lyte Innovations.

2.3. Electrolyte formulation and cell assembly

1 M $LiPF_6$ in EC:EMC (3:7, by vol.) was used as a baseline electrolyte (BE). All considered electrolytes were formulated by adding the molar ratio of salts and additives and amounts of co-solvents VC/PFPN/CF_3PFPN by weight percentage to an EC:EMC (3:7 by vol.) stock solution in a volumetric flask. The resulting electrolyte formulations were stored in the argon-filled glovebox. All considered cells were assembled in an argon-filled glovebox (MBraun Labmaster, H_2O and O_2 content <0.5 ppm). For all galvanostatic cycling measurements, 2032-type two-electrode coin cells (cathode ø 14 mm, anode ø 15 mm) with one layer of Celgard 2500 separator (ø 16 mm), 35 µL of electrolyte and two spacers with a thickness of 0.5 mm and 1 mm were assembled. For cyclic voltammetry measurements (CV), 3-electrode Swagelok T-cells with one layer of Whatman grade GF/D (ø 13mm and 10 mm) as the separator, and 200 µL of electrolyte were assembled with Si-Gr or NMC811 electrodes as a working electrode and Li metal as counter and reference electrodes.

2.4. Self-extinguishing time determination

Flammability tests were conducted within a fume hood, maintaining consistency by marking the positions of both the sample stand and the lighter. Each test involved applying 400 µL of the sample onto a stack comprising four layers of fiberglass discs (Whatman GF/D, ø 12 mm, and 0.67 mm thick) suspended on a needle. A regular household lighter with a long nozzle positioned on a stand, was placed at a distance of 3.5 cm from the burner head to the sample (**Figure S15**). Samples were ignited for 10 s, and the burn time, excluding the ignition time, was used to calculate the self-extinguishing time (SET), which was obtained by dividing the burning time by the electrolyte mass.

2.5. Electrochemical impedance spectroscopy

Electrochemical impedance spectroscopy (EIS) measurements were carried out with a potentiostat workstation (VMP3, BioLogic, France). First, two-electrode cells were galvanostatically cycled for three formation cycles, then based on the work of Petibon et al.[27] charged to 50% state of charge (SOC). Symmetric cell impedance was measured at a range of 1MHz - 10 mHz after 30 min of rest time.

Thereafter, the coin cells were disassembled, symmetric cells with 35 µL of the fresh electrolyte were reassembled, and impedance spectra of the symmetric cells were recorded[26].

2.6. Attenuated total reflection Fourier-transform infrared spectroscopy

Attenuated Total Reflection Fourier-Transform Infrared (ATR-FTIR) spectroscopy analysis of the interphases on the electrode surfaces was conducted on an Invenio-R FT-IR spectrometer (Bruker) with a Platinum-ATR unit (diamond crystal, Bruker) and a mercury-cadmium-telluride (MCT) detector inside a custom-made glovebox under nitrogen flux. The coin cells were galvanostatically cycled for 3 formation cycles, opened afterwards under inert atmosphere in a glovebox and transferred to the IR spectrometer under inert atmosphere. To minimize sample contamination and maintain the integrity of the formed SEIs and CEIs, the electrodes were not washed. The spectra were acquired with a spectral resolution of 4 cm^{-1} at an incidence angle of 45°. Each spectrum was obtained by accumulating 32 interferograms for background and sample spectra, respectively. The spectra are presented in the form of absorbance and were processed by concave rubber band background correction (15 iterations, straight lines).

2.7. Gas chromatography-mass spectroscopy

Cells were galvanostatically cycled, and thereafter disassembled in a glovebox. The electrolyte was extracted by centrifuging soaked separator and electrodes (15 min, 14 500 rpm). After centrifugation, a volume of 10 µL of electrolyte was injected into 20 mL headspace vial in a dry room (dew point <-65 °C, H_2O content < 6 ppm). Sample extraction was carried out by solid-phase microextraction (SPME) using polyacrylate fiber (85 µm, Restek).

For gas chromatography-single quadrupole mass spectrometry (GC-SQMS), Shimadzu QP2010 Ultra equipped with AOC-5000 autosampler and standard non-polar Supelco SLB-5 ms column (30 m x 0.25 mm x 0.25 µm, Sigma Aldrich) was used in electron ionization mode (EI) in a range of 20-350 m/z. SPME sampling was carried out for 10 s (split 1:100) and 600 s (split 1:10). Other GC and MS parameters were set according to Mönninghoff et al.[28] Compound identification was done by spectral comparison with NIST 11 library.

For gas chromatography-high resolution mass spectrometry (GC-HRMS), TRACE 1310 Series GC hyphenated to Q Exactive Orbitrap MS (Thermo Fisher Scientific, USA) was used. Sample diluted in dichloromethane (1:100) was introduced into GC injector with a split of 1:5. The column flow and GC oven settings were identical to SQMS measurement. The mass spectrometer was run in EI or positive chemical ionization (PCI) mode, the ion source and transfer line temperatures were held at 230 and 250 °C, respectively. Ammonia was used as a reagent gas with flow of 1.5 mL/min for CI mode. For both ionization modes, mass range was set to 50–500 m/z with an automatic gain control target of $1 \cdot 10^6$ and a resolution of 60 000.

2.8. Scanning electron microscopy & energy-dispersive X-ray spectroscopy

An Auriga electron microscope (Carl Zeiss, Microscopy GmbH, Germany) was used for scanning electron microscopy (SEM) imaging.

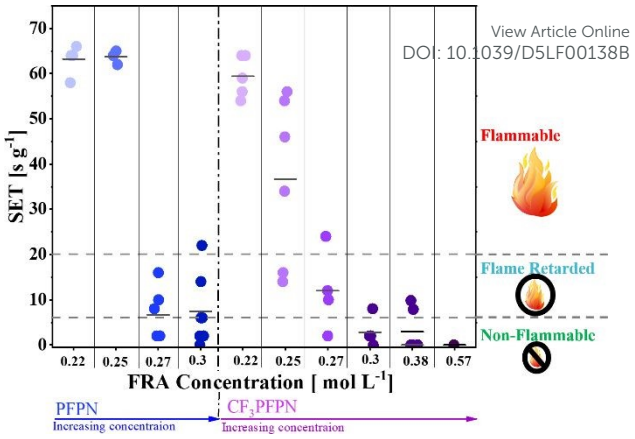

Figure 2. SET Values determined for electrolyte compositions containing different concentration of PFPN and CF_3PFPN in BE (EC:EMC 3:7 vol. + 1.0 M $LiPF_6$)+ 0.038 M PhEPi + 8 % VC. Details on the sample number are summarized in **Table 1**.

The micrographs were obtained with an accelerating voltage of 3 kV and a working distance of 5 mm. Energy-dispersive X-ray spectroscopy (EDX) measurements were carried out at an accelerating voltage of 10 kV using an energy-dispersive X-ray detector (Oxford Instruments, UK). The electrodes were harvested from a NMC811||Si-Gr (20 % Si) coin cell containing the considered electrolytes and compared with the pristine electrodes. Prior to SEM and EDX measurements, the electrodes were rinsed with 1 mL EMC in an argon-filled glovebox, dried under reduced pressure, and transferred in an air-tight sample chamber.

Results and Discussion

3.1. Evaluation of flame-retardant additives in the electrolyte

To comprehensively evaluate the FRAs, it is imperative to conduct thorough investigations at the electrolyte level, particularly focusing on flammability. Evaluating this property not only ensures the safety of the resulting cell chemistries but also determines their reliability under diverse conditions, such as elevated temperatures and high-voltage operations.

The flammability of the electrolytes is typically evaluated by the SET, which refers to the duration for continuous burning of an ignited sample after the removal of the ignition source per gram of sample. Based on the SET values, electrolytes are categorized into three groups[24,29]: (i) Non-flammable electrolytes (SET < 6 s g^{-1}), (ii) Flame

Table 1. Summarized results obtained from SET determination in **Figure 2**

Molar concentration of FRAs in electrolyte formulation [mol L^{-1}]	Concentration of FRAs in electrolyte [wt.%]	Mean SET value [s g^{-1}]
PFPN		
0.22	4.9	64
0.25	5.6	64
0.27	6.0	7
0.30	6.7	8
CF_3PFPN		
0.22	5.8	60
0.25	6.6	41
0.27	7.2	12
0.30	7.9	3
0.38	10	3
0.57	15	0

View Article Online
DOI: 10.1039/D5LF00173B

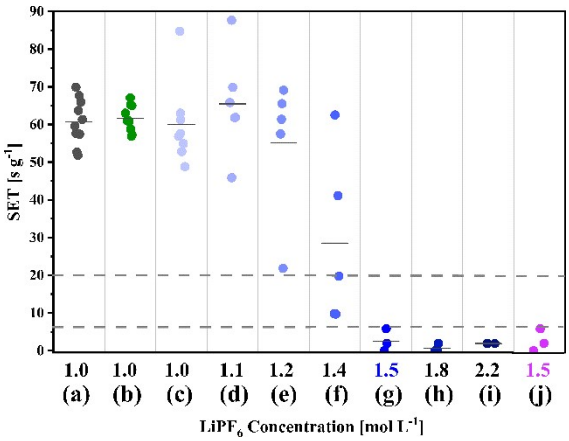

Figure 3. SET Values of electrolytes containing $LiPF_6$ in different concentrations (a) BE, (b) BE + VC + PhEPi (c-i) different molar concentration of $LiPF_6$ in EC:EMC 3:7 vol.+ 5 % PFPN + 8 % VC + 0.038 M PhEPi (j) 1.5 M LiPF6 in EC:EMC 3:7 vol.+ 5 % CF3PFPN + 8 % VC + 0.038 M PhEPi.

retarded electrolytes (6 s g^{-1} < SET < 20 s g^{-1}), and (iii) Flammable electrolytes (SET > 20 s g^{-1}).

Figure 2 shows the SET determination results of the electrolytes containing the two FRAs; PFPN and CF_3PFPN. Regarding the difference in molecular weight between the two FRAs (M_{PFPN}: 275 g mol^{-1} , $M_{CF3PFPN}$: 328.96 g mol^{-1}), a fair comparison was conducted based on the molar concentrations.

The concentration range for PFPN was chosen based on previous studies[14,15,30–32], which suggested a starting point of 5 wt. % which corresponds to ≈ 0.22 mol L^{-1} PFPN and 0.19 mol L^{-1} CF_3PFPN. The obtained data is shown in **Figure 2** and summarized in **Table 1**. It was found that achiving a non-flammable electrolyte containing PhEPi and VC requires minimum 0.3 M of CF_3PFPN and more than 0.3 M of PFPN. Therefore, CF_3PFPN with lower molar concentration has a better efficiency compared to the counterpart.

Several studies show that increasing the concentration of inorganic components like inorganic additives or conducting salt in electrolytes has a considerable impact on how flammable and safe the resulting electrolytes are, as well as how long their impact on flammability will last[33–35]. High concentrations of conducting salt in electrolyte can enhance its non-flammability through several mechanisms, including a reduction in the amount of free, flammable solvent due to extensive salt solvation, and increase in electrolyte viscosity that hinders rapid solvent vaporization[36,37]. While these effects can improve safety, it is crucial to consider potential drawbacks such as increased viscosity, which can negatively impact ionic conductivity and cell performance. To achieve a non-flammable electrolyte with minimal use of FRA, an alternative approach was taken by optimizing the $LiPF_6$ concentration instead of increasing the FRA concentration beyond 5 %. As shown in Figure 3, 1.5 M of $LiPF_6$ in EC:EMC containing 5 wt. % PFPN or CF_3PFPN, 0.038 M PhEPi and 8 wt. % VC results in a non-flammable electrolyte formulation. Subsequently, 1.5 M $LiPF_6$ in EC:EMC will be referred to as BE_2. This strategy enabled preservation of the electrolyte's performance by avoiding potential negative impacts associated with elevated FRA levels while also achieving a more cost-effective formulation.

3.2. Electrochemical characterization of non-flammable electrolyte formulations

In order to evaluate the electrochemical stability of FRAs and their impact on electrolyte performance under typical LIBs operating conditions, cyclic voltammetry (CV) measurements were performed from 0.01 to 5.0 V *vs.* $Li|Li^+$ for BE + 5 % FRA formulations (**Figure S1**). No oxidative decomposition of FRAs was observed up to 5.0 V on NMC811 electrodes, and no electrochemical reduction occurred on Si-Gr until 0.01 V *vs.* $Li|Li^+$, aligning with previous studies on fluorocyclophosphazenes[19,30,38]. These results confirm the electrochemical stability of PFPN and CF_3PFPN within standard LIB voltage ranges.

Considering the electrochemical stability of these two cyclophosphazenes, the impact of the FRAs on the cell performance was evaluated as well. NMC811||Si-Gr cells (20 % Si) containing electrolytes with 5% of each FRA respectively in BE + PhEPi + VC were galvanostatically cycled for 100 cycles up to 4.2 V cut-off voltage, as

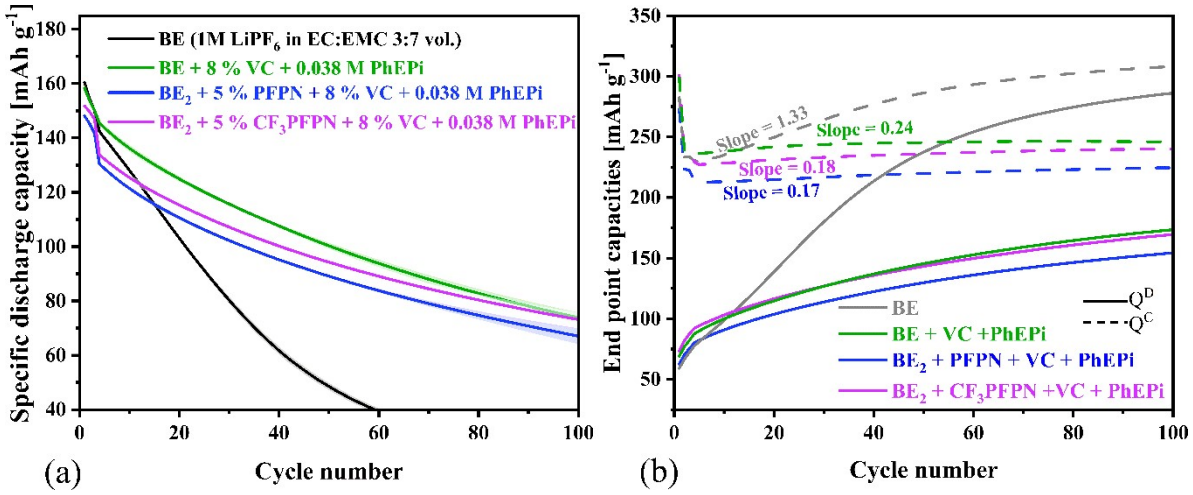

Figure 4. (a) Specific discharge capacities of NMC811||Si-Gr cells with considered electrolytes as a function of the cycle number (b)The charge and discharge endpoints of the considered electrolytes are plotted *versus* cycle number.

View Article Online
DOI: 10.1039/D5LF00138B

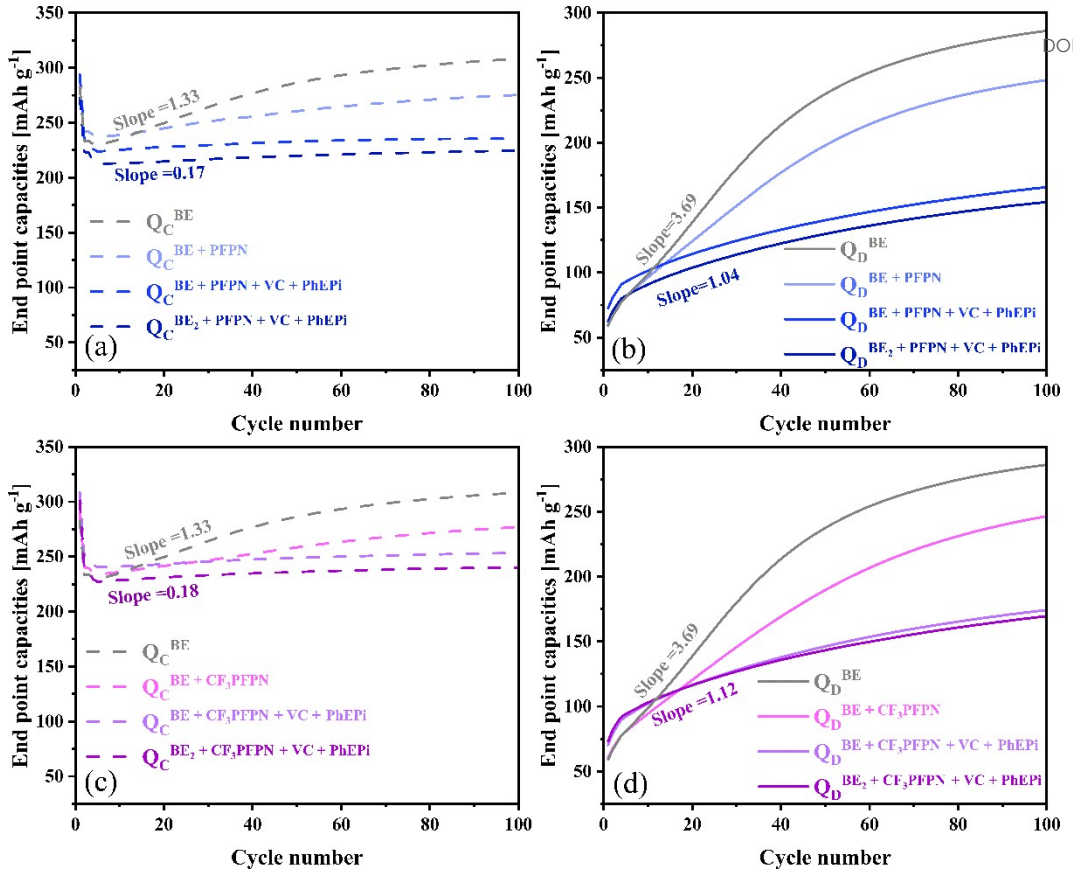

Figure 5. (a) Endpoint charge capacity *vs.* cycle number graph for NMC811||Si-Gr cells with and without PFPN, (b) The endpoint discharge capacity graph for NMC811||Si-Gr cells containing electrolytes with and without PFPN, (c) The endpoint charge capacity *vs.* cycle number graph for NMC811||Si-Gr cells containing electrolytes with and without CF_3PFPN, (d) The endpoint discharge capacity graph for NMC811||Si-Gr cells containing electrolytes with and without CF_3PFPN.

shown in **Figure 4**. The specific discharge capacities of cells with the considered electrolytes as a function of cycle number is presented in **Figure 4a**, comparing BE to advanced electrolyte formulations with and without FRAs. There is a substantial initial capacity loss for cells containing BE during the formation cycles. This decline is primarily attributed to the loss of lithium inventory resulting from substantial volume change of the Si-based negative electrode during SEI formation in the NCM811||Si-Gr cells [39–42], which leads to rapid capacity decay in the subsequent cycles. As prevoiusly reported, the addition of PhEPi and VC as film forming additives to BE leads to an improvement in electrochemical cell performance both in terms of discharge capacity as well as capacity retention[26]. Addition of FRAs, combined with increased $LiPF_6$ concentration (BE_2), results in a decline in intial capacities for both electrolyte containing PFPN and CF_3PFPN compared to the electrolyte with BE as well as PhEPi + VC. However, in the cells containing CF_3PFPN, the accumulated specific discharge energy (ADE) improved from 22 Wh g^{-1} to 34 Wh g^{-1} after 100 cycles compared to the cells with BE, showcasing an enhancement in capacity retention and galvanostatic cycling performance. This improvement suggests that CF_3PFPN contributes to improved stability and efficiency of the electrolyte, likely by improving interphase properties and reducing capacity fading compared to the BE. In comparison, the ADE of the cell containing CF_3PFPN shows very similar behaviour to the cell with PhEPi + VC (37 Wh g^{-1}). In contrast, electrolyte containing PFPN results in lower discharge capacity compared to cells containing CF_3PFPN and ADE of 32 Wh g^{-1} after 100 cycles.

The variations in charge and discharge capacity endpoints *vs.* cycle number can indicate side reactions at the cathode and anode, respectively.[43] **Figure 4b** shows the charge and discharge capacity endpoints *vs.* cycle number, calculated by taking the corresponding cumulative capacity values [42–44]. As shown in this figure, the charge capacity endpoint (Q_C) of BE increases with a slope of 1.33 between the 4th and 40th cycle. The marching of Q_C indicates oxidation side reactions on the positive electrode, leading to the growth of cumulative capacity to larger values than the theoretical capacity. On the other hand, the discharge capacity endpoint (Q_D) of BE also marches to higher values during continued galvanostatic cycling. The large value of the slope may indicate a high magnitude of side reactions resulting from ineffective SEI formation or increased dead lithium due to lithium metal plating at the negative electrode. The cells containing PhEPi and VC show a much lower slope for Q_D and Q_C as presenting in **Figure 4b** indicating a classical aging, which means that Q_D and Q_C endpoints slowly converge[42]. Cells containing PhEPi, VC and FRAs additives, CF_3PFPN and PFPN, demonstrate slower marching between Q_C and Q_D endpoints compared to the cells without them and the reduced slopes can be attributed to the reduction of side reactions on positive electrodes. **Figures 5a-d**, illustrate Q_C and Q_D upon stepwise incorporation of the additives and conducting salt concentration in the baseline electrolyte. As it can be seen in **Figure 5a**, the slope of Q_C is decreased to 0.17 from 1.33 when

View Article Online
DOI: 10.1039/D5LF00138B

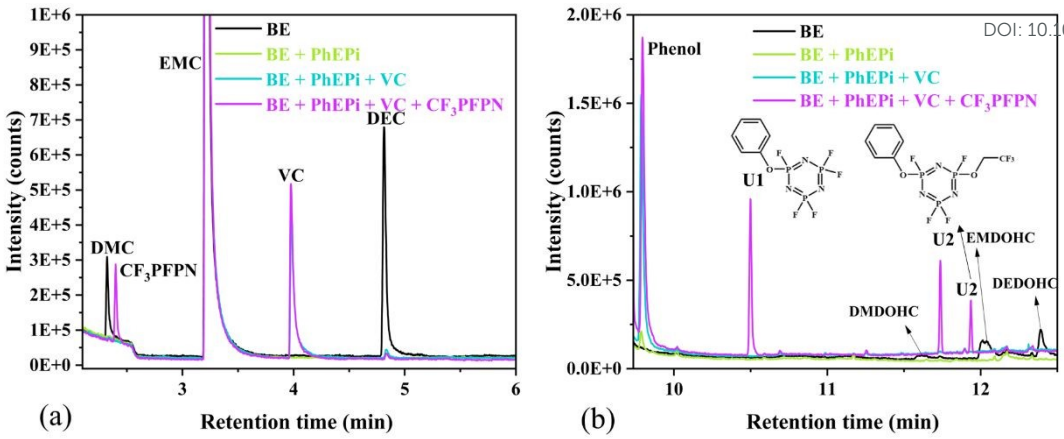

Figure 6. (a) Gas chromatograms obtained from 10 s SPME sampling of extracted BE or electrolyte containing PhEPi, PhEPi + VC or PhEPi + VC + CF_3PFPN (b) Gas chromatograms obtained from 600 s SPME sampling of extracted BE or electrolyte containing PhEPi, PhEPi + VC or PhEPi + VC + CF_3PFPN. The postulated structures of the compounds are represented in the figures at the retention time of the corresponding peaks.

PFPN with PhEPi and VC are added to the BE. **Figure 5c** illustrates the similar behavior for CF_3PFPN with PhEPi and VC. It can be concluded that by presence of each of these two FRAs, the oxidation side reactions on positive electrodes have been considerably decreased. Moreover, higher $LiPF_6$ concentration does not affect the slope of Q_D and Q_C, but results in a reduction of endpoint capacities, as evidenced by the decrease in discharge capacity observed in **Figure 4a**. From this point it can be concluded that a higher amount of $LiPF_6$ has no impact on the side reactions on the positive electrode. A similar behavior is observed for the discharge endpoint capacities in **Figure 5b** and **d**, suggesting that the presence of additives reduces the side reactions on the negative electrode. Additionally, the increased amount of $LiPF_6$ has no considerable impact on the side reactions at the negative electrode.

3.3. Electrolyte investigation by gas chromatography-mass spectrometry

The enhancement achieved by incorporating FRAs has directed the focus toward investigation of the changes in electrolyte composition during galvanostatic cycling. The electrolyte was extracted from cells after the first charge/discharge cycle and analyzed by gas chromatography-single quadrupole mass spectrometry (GC-SQMS) to gain insights into the changes in electrolyte composition. The GC-SQMS results from analyzing the electrolyte extracted from the cell with CF_3PFPN are compared to those from the cells without it. **Figure 6a** and **b** show the gas chromatogram of the electrolyte for 10 s and 600 s using head-space solid-phase microextraction (SPME) method. A 10 s extraction focuses on immediate, volatile, or transient species, whereas a 600 s extraction provides a more complete and detailed analysis of all the long-term extractable components.

Analysis of the chromatograms, depicted in **Figure 6a**, reveals reduced amounts of DMC and DEC at retention times of 2.3 and 4.8 min for all samples containing additives, including CF_3PFPN. This can be attributed to less side reactions at the electrodes and suppressed decomposition of EC and EMC, thereby preventing the formation of transesterification products such as DMC and DEC. Therefore, less active lithium loss may be observed, leading to improved capacity retention[45,46] as evidenced by the electrochemical performance of the cells (**Figure 4a**). The gas chromatograms acquired at 600 s extraction time revealed presence of additional compounds (**Figure 6b**). These compounds were found in samples containing CF_3PFPN with retention times of 10.5 (U1), 11.7 and 11.9 min (U2) in the chromatogram, the latter two having identical mass spectra. It is assumed that these unknown compounds consist of a phenoxy group attached to phosphazene ring (U1) or to CF_3PFPN (U2). The two compounds with identical mass spectra are likely stereoisomers (*cis*/*trans* or conformational). The presence of phenoxy groups in phosphazene-based degradation compounds confirms the expected PhEPi decomposition. Other compounds that were found in the chromatogram of BE samples after 600 s extraction, are dioxahexane dicarboxylates, namely dimethyl dioxahexane dicarboxylate (DMDOHC, (a) at 11.6 min), ethyl methyl dioxahexane dicarboxylate (EMDOHC, (b) at 12.0 min) and diethyl dioxahexane dicarboxylates (DEDOHC, (c) at 12.4 min), which are by-products of electrolyte decomposition and are called OHCs[47,48] for short. Their presence is detrimental to the cell performance as a results of electrolyte consumption, Analysis of the chromatograms, depicted in **Figure 6a**, reveals reduced amounts of DMC and DEC at retention times of 2.3 and 4.8 min for all samples containing additives, including CF_3PFPN. This can be attributed to less side reactions at the electrodes and suppressed decomposition of EC and EMC, thereby preventing the formation of transesterification products such as DMC and DEC. Therefore, less active lithium loss may be observed, leading to improved capacity retention[45,46] as evidenced by the electrochemical performance of the cells (**Figure 4a**). The gas chromatograms acquired at 600 s extraction time revealed presence of additional compounds (**Figure 6b**). These compounds were found in samples containing CF_3PFPN with retention times of 10.5 (U1), 11.7 and 11.9 min (U2) in the chromatogram, the latter two having identical mass spectra. It is assumed that these unknown compounds consist of a phenoxy group attached to phosphazene ring (U1) or to CF_3PFPN (U2). The two compounds with identical mass spectra are likely stereoisomers (*cis*/*trans* or conformational). The presence of phenoxy groups in phosphazene-based degradation compounds confirms the expected PhEPi decomposition. Other compounds that were found in the chromatogram of BE samples after 600 s extraction, are dioxahexane dicarboxylates, namely dimethyl dioxahexane dicarboxylate (DMDOHC, (a) at 11.6 min), ethyl methyl dioxahexane dicarboxylate (EMDOHC, (b) at 12.0 min) and diethyl

View Article Online
DOI: 10.1039/D5LF00138B

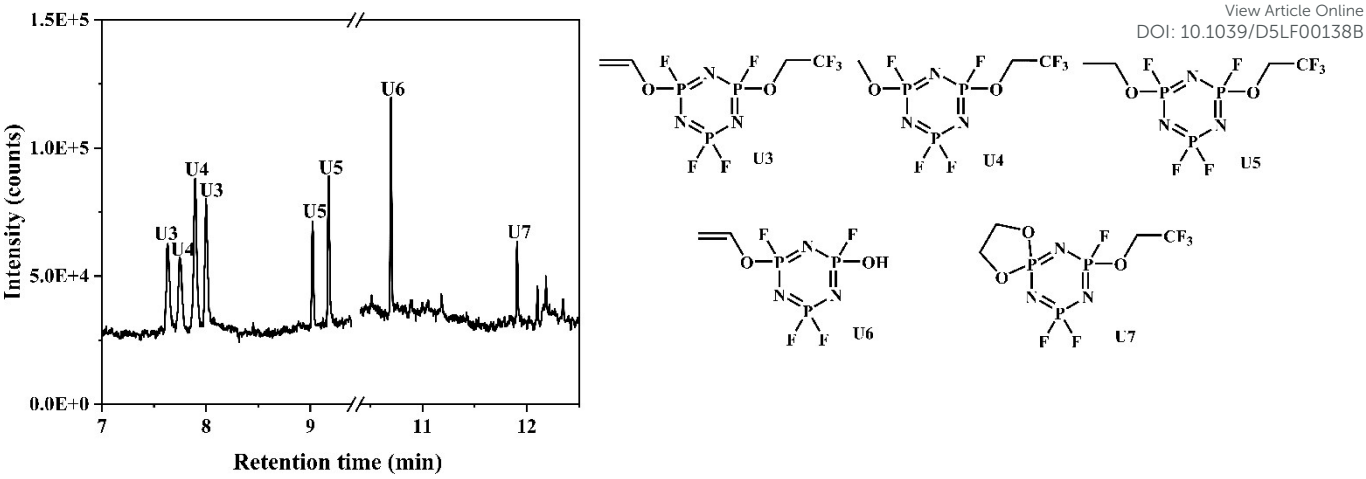

Figure 7. Gas chromatogram obtained from sampling of extracted BE + CF_3PFPN electrolyte and the representation of the postulated structures of U3-U7 compounds.

dioxahexane dicarboxylates (DEDOHC, (c) at 12.4 min), which are by-products of electrolyte decomposition and are named OHCs[47,48] for short. Their presence is detrimental to the cell performance as a results of electrolyte consumption, forming less effective interphases, and contributing to gas generation[49–51]. However, minimizing the formation of such by-products in additive-containing samples, indicates the positive impact of additives.

An interesting phenomenon was observed for the cells containing only CF_3PFPN in BE. As a result, many new decomposition products emerged in the gas chromatogram, which have not been previously observed in BE + PhEPi + VC + CF_3PFPN sample (**Figure 7**). With the help of gas chromatography-high resolution mass spectrometry (GC-HRMS), several phosphazene-based structures are proposed (**Figure 7**). The differences in degradation products observed when PhEPi and VC were absent, suggest that these additives played a role in preventing degradation of CF_3PFPN. Furthermore, the GC-HRMS analysis that aimed at typical carbonate degradation fragment ($C_5H_9O_3$, exact mass 117.0546)[52], revealed two compounds (U4 and U5) in **Figure 7**. These compounds (U4 and U5), which are CF_3PFPN degradation products, are structurally similar to those described by Ghaur et al.[52] who used PFPN as additive. To have a direct comparison between PFPN and CF_3PFPN in the bulk electrolyte, additional experiments with cells containing BE + PFPN were conducted. GC-HRMS measurement suggested that CF_3PFPN-derived compounds U3, U4, U5, and U6 share structural similarities with the PFPN-derived counterparts U8, U9, U10, and U11 as depicted in **Figure 8**. It is noteworthy that none of these compounds was found in the chromatogram of VC + CF_3PFPN samples, which proved the effect of VC addition on suppressing the evolution of carbonate and phosphazene degradation compounds. The other postulated structure U7 as CF_3PFPN-derived compound was specifically formed from its respective compounds and has no analogous structures in the other system.

Phosphazene-based additives undergo chemical reactions with the decomposition products of other electrolyte components, while the core phosphazene ring remains intact. These reactions are likely not electrochemical in nature, since these changes are not reflected in the current profiles of voltammograms for PFPN and CF_3PFPN, whether on NMC811 or Si-Gr electrodes. It is assumed that phosphazene-based additives indirectly contribute to CEI (cathode electrolyte interphase [53]) and SEI (solid electrolyte interphase[54]) formation by scavenging some of the decomposition species

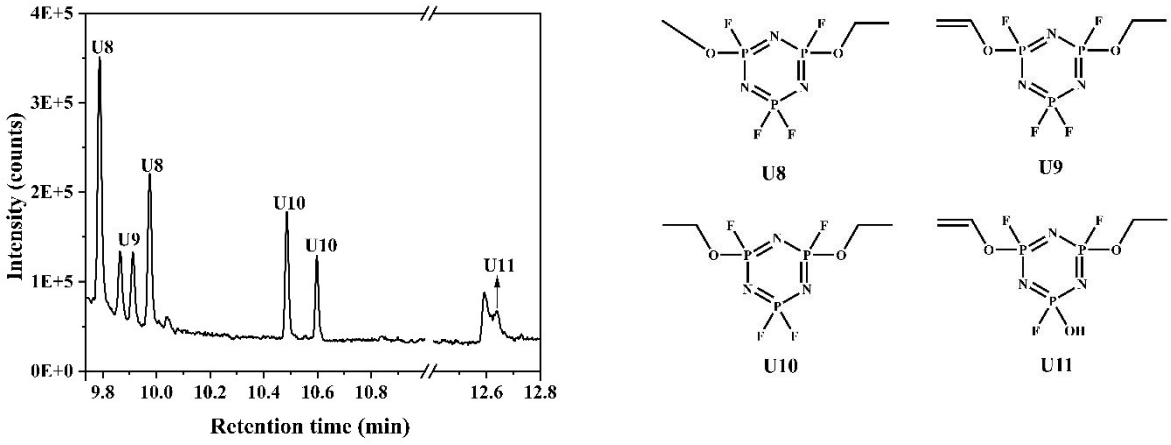

Figure 8. Gas chromatogram obtained from sampling of extracted BE + PFPN electrolyte and the representation of the postulated structures of U8-U11 compounds.

View Article Online
DOI: 10.1039/D5LF00138B

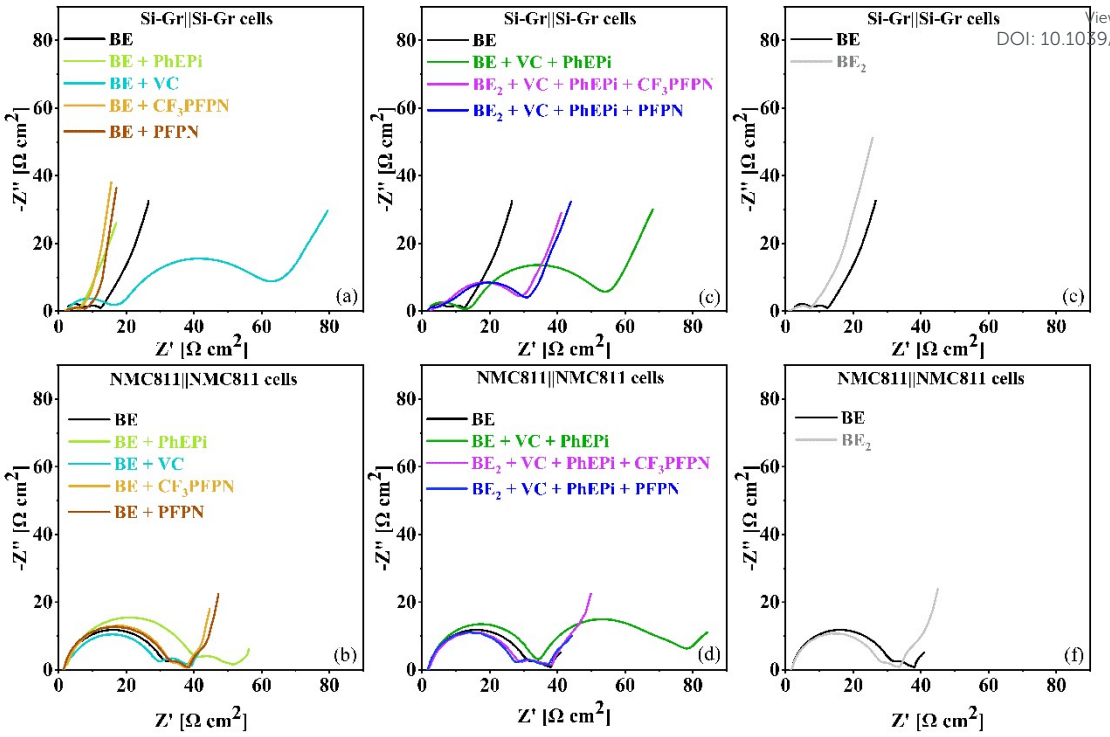

Figure 9. (a)(b)(c) Nyquist plots of symmetric Si-Gr|| Si-Gr cells assembled from galvanostatic cycled NMC811||Si-Gr cells, (d)(e)(f) Nyquist plots of symmetric NMC811||NMC811 cells assembled from harvested NMC811 and Si-Gr electrodes.

generated from the other electrolyte components. This scavenging action minimizes the formation of OHCs, which consequently leads to formation of more effective SEI and CEI. Additionally, the differences in galvanostatic cycling performance of cells containing CF_3PFPN and PFPN, appear to stem from the variations in the degradation products of these two additives, as discussed in the GC-MS results. Thereby, a more improved galvanostatic cycling performance of cell containing CF_3PFPN compared to its counterpart is observed.

3.4. The impact of phosphazene-based additives on SEI and CEI composition

To understand the interactions of additives toward the formation of the SEI/CEI, incorporating impedance measurements allows a detailed assessment of interfacial resistance changes and stability over time. The Nyquist plots of symmetric NMC811 and Si-Gr cells assembled from galvanostatically cycled NMC811||Si-Gr cells with the considered electrolyte formulations are shown in **Figure 9**. In all plots two semicircles were observed. The first semi-circle is representative of interphase resistance at high frequencies and the second semi-circle at medium frequencies is representative of the charge transfer resistance at the electrode|electrolyte interface[55–60]. **Figure 9a** and **b** illustrate the impact of electrolytes containing additive on negative and positive electrode impedance compared to BE, respectively. It can be observed that on Si-Gr the addition of FRAs to BE, results in impedance reduction. However, the biggest changes come from VC on Si-Gr, especially on the second semi-circle as discussed in the reported paper[26], due to the formation of poly(VC) and reduced charge transfer efficiency[39,61,62]. It was also concluded that PhEPi plays the dominant role on NMC811 electrode, due to the higher interphase resistance which is observable in **Figure 9b**. **Figure 9e** and **f** illustrate the influence of $LiPF_6$ concentration on impedance of symmetric Si-Gr||Si-Gr cells and symmetric NMC811||NMC811 cells, respectively, which leads to a small decrease in cell resistance containing 1.5 M $LiPF_6$ (BE_2). The results displayed in **Figures 9c** and **9d**, show that FRAs combined with PhEPi and VC contribute to lowering the impedance in the symmetric cells compared to the impedance of symmetric cells with PhEPi + VC. As discussed in the previous sections, this reduction in impedance specially in the second semi-circle likely results from reduced undesired electrolyte decomposition such as OHCs due to the presence of FRAs in combination with PhEPi and VC. This combination leads to less side reactions, and contribute to forming a more conductive SEI composition, all of which enhances the overall efficiency of the formed interphases.

3.5. SEI investigation by ATR-FTIR spectroscopy

To further investigate the impact of CF_3-group in CF_3PFPN on the SEI layer, ATR-FTIR analysis was carried out on the electrolytes and the NMC811 and Si-Gr electrodes, which were harvested from the cells at 80 % state of health (SOH). The IR spectra of the SEI on Si-Gr electrode formed with electrolyte containing PFPN or CF_3FPFPN with PhEPi and VC, show substantial differences compared to the spectrum of SEI formed with the BE electrolyte. This is mostly due to the addition of VC[26], leading to poly(VC) formation[61,63,64]. The presence of VC to the electrolyte formulation also leads to the suppression of lithium alkyl carbonates ($ROCO_2Li$) formation, indicated by the band at 1640 cm^{-1}[63,65] (**Figure 10e-f**). Suppression of $ROCO_2Li$ formation, indicates a reduction in lithium loss inventory and electrolyte consumption, which prevents gas evolution, and

View Article Online
DOI: 10.1039/D5LF00138B

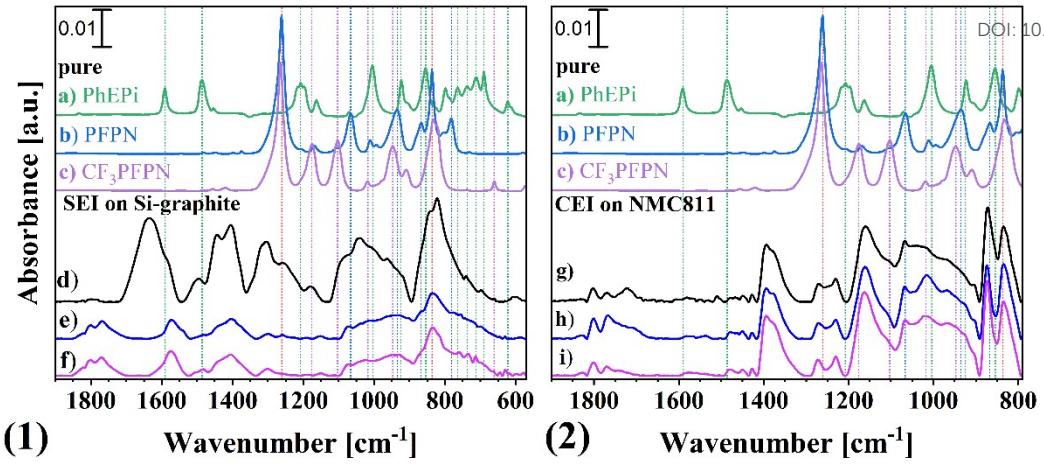

Figure 10. ATR-FTIR spectra of (1) SEI on Si-graphite and (2) CEI on NMC811 electrodes after cycling, compared with spectra of the pure additives: a) PhEPi, b) PFPN, and c) CF_3PFPN. The electrodes were extracted from cells containing: d, g) baseline electrolyte (BE), e, h) BE_2 + PFPN + VC + PhEPi, and f, i) BE_2 + CF_3PFPN + VC + PhEPi. Spectral features corresponding to each additive and interphase evolution are highlighted. Detailed band assignments are provided in the Supporting Information (SI)

helps to maintain an effective SEI. This can explain the improvement in capacity fading observed in **Figure 4a**.

In the pristine spectrum of PhEPi (**Figure 10a-a**), vibrational bands at 1590 cm^{-1}, and 1486 cm^{-1}, can be assigned to E_{2g} and E^*_{1u} of the phenol ring.[66,67] In the spectra of the formed SEI with electrolytes containing PhEPi, the band 1590 cm^{-1} might overlap with BE or VC decomposition products, such as carboxylates (RCOOLi).[63] However, the presence of small bands at 1482, 1070, 828, 764, 623, and 612 cm^{-1} in **Figure 10e-f** spectra also indicate the presence of phenol ring in the formed SEI compared to the pure PhEPi spectrum.

Furthermore, bands at 1007, 924, and 713, cm^{-1} in the spectra of the formed SEI with electrolytes containing PhEPi and PFPN or CF_3FPFPN as electrolyte additives indicate the presence of phospholane part. The two intense bands of PhEPi at 854 cm^{-1} (ν P-O(Ph)) and 1198 cm^{-1} (ν PO-C(Ph)), which indicate the intact PhEPi, cannot be clearly identified in **Figure 10e** and **f**. In both spectra of PFPN and CF_3FPFPN, the two bands at 1261 (ν P-N) and around 835 cm^{-1} (ν_s F-P(O) or ν_s CF_3), as shown by red lines, are the most intense in the spectra of the pristine component. These bands are also present in the SEI spectra of the Si-Gr electrode extracted from the cells containing PFPN or CF_3FPFPN. However, similar bands are also detected in the SEI spectrum formed by BE, making clear identification difficult. Nonetheless, the pure component spectra reveal distinct bands that cannot be identified and distinguished in the SEI spectra. These bands are at 1066 (CH_2 + δ_{as} bend CH_3), 865 (ν_s P-F), and 783 cm^{-1} (ν_s P-F) for pure PFPN and at 1182 (δ CF_3 + δ_r CH_2), 1025 (ν_{as} P-O-C), and 661 cm^{-1} (δ_i CF_3) for pure CF_3PFPN.

3.6. CEI investigation by ATR-FTIR spectroscopy

Comparing the spectrum of the formed CEI in BE with the spectra of the formed CEI in electrolytes containing VC, PhEPi, and PFPN and CF_3FPFPN shows diminishing bands at 1722, 1510 and 1247 cm^{-1}, in presence of additive mixture, whereas a new prominent band appears at 1016 cm^{-1}. The diminishing bands at 1722, 1510, and 1247 cm^{-1} can be attributed to the ν C=O, δ CH_2, and ν C(O)-O vibrations of EC or EMC decomposition products, which are thus formed less in the presence of VC, PhEPi, and PFPN or CF_3FPFPN additives, due to an enhanced electrode protection. In comparison with the spectra of the bulk components previous investigation with shell-isolated nanoparticle-enhanced Raman spectroscopy, the band at 1016 cm^{-1} can be assigned to PhEPi[26]. Thus, it is indicated that small amounts of intact PhEPi might be present in the CEI. This supports the suggestion of PhEPi decomposition mechanism on NMC811 electrode to phenol and poly(phosphate)[68]. However, bands that can be assigned to PFPN or CF_3FPFPN could not be identified clearly. It can be concluded that the phosphazene-based additives or their decomposition products are not present on electrodes, which means that they do not contribute to the CEI structure and, as they are soluble, they can be found in the bulk electrolyte.

Energy dispersive X-ray spectroscopy (EDX) analysis of the extracted cathodes and anodes from the NMC811||Si-Gr cells containing PFPN or CF_3FPFPN alongside with PhEPi and VC at 80% SOH compared to the cells with PhEPi and VC (**Figure S10**) did not reveal any nitrogen peaks or considerable changes in the phosphorus atomic concentration. This can support the ATR-FTIR results where no degradation or intact species of PFPN or CF_3PFPN were observed. It is necessary to mention that no obvious oxidation/reduction peak could assign as a decomposition in the voltammograms of electrolytes containing PFPN/CF_3PFPN on NMC811 and Si-Gr electrodes but different chemical decomposition products of PFPN and CF_3PFPN were found in the bulk electrolyte.

Conclusion

The formulation of targeted electrolyte additive mixtures (“additive package”) for optimum performance and/or specific applications of the resulting cell chemistries is a fruitful R&D topic in both academia and industry. Building upon the established synergistic benefits of VC and PhEPi in NMC811||Si-graphite cells, this study successfully integrated CF_3PFPN, a cyclotriphosphazene-based flame retardant to achieve non-flammable electrolyte with minimal compromise to electrochemical performance. A key finding was the higher efficiency of the fluorinated CF_3PFPN, requiring a lower molar concentration (minimum 0.3 M) to achieve non-flammability compared to PFPN (greater than 0.3 M). Final formulations using concentration of 0.22 mol L^{-1} PFPN or 0.19 mol L^{-1} CF_3PFPN (both 5 wt.%) combined with increased conducting salt concentration (1.5 M) provided an

effective balance between safety and performance. While the fluorinated CF_3PFPN exhibited only marginal performance improvements over its non-fluorinated counterpart, PFPN, *post mortem* analyses revealed a crucial indirect role for both in modulating SEI and CEI composition by effectively scavenging detrimental alkoxide species, which is a key factor in long-term stability. These findings highlight the value of well-designed additive packages, particularly those incorporating phosphazenes, to simultaneously enhance both the safety and longevity of high-energy lithium-ion batteries, paving the way for their more reliable and widespread application, especially in systems utilizing silicon-rich anodes.

Author contributions

B.A.S. carried out the majority of the experiments and data analysis. I.C.-L. and M.W. supervised the project, acquired funding, and contributed to project administration. C.W. and B.A.S. wrote the initial draft of the manuscript with input from I.C.-L. and other co-authors. M.S., M.We., M.B. and S.N. contributed to formal analysis and methodology. J.M., S.K., M.St., and M.We. supported the investigation and characterization work. M.St. and G.-V.R. synthesized and provided the phosphazene additives. M.G. and M.S. assisted with data interpretation. All authors reviewed the manuscript and approved its final version.

Conflicts of interest

There are no conflicts of interest to declare.

Data availability

The data that support the findings of this study are available on request from the authors.

Acknowledgements

This project has received funding from the European Union's Horizon 2020 research and innovation program under grant agreement No 875548. The authors gratefully acknowledge Matjaž Koželj, Alix Ladam, and Sébastien Fantini from Research and Innovation Department of Solvionic, for scaling up the new additives and Andre Bar for the graphical abstract.

References

[1] K. Shrikaant, K. Boris, H. A.K, S. Vipul, *Next Generation Materials for Sustainable Engineering*, IGI Global, **2024**.

[2] Afzal, O. D. Silva, M. Bhurt, S. Sajnani, S. Maniama, in *Batter. Future Energy Storage*, Jenny Stanford Publishing, **2024**.

[3] S. Passerini, L. Barelli, M. Baumann, J. Peters, M. Weil, Eds. , *Emerging Battery Technologies to Boost the Clean Energy Transition: Cost, Sustainability, and Performance Analysis*, Springer Nature, **2024**.

[4] Z. Ye, J. Li, Z. Li, *J. Mater. Chem. A* **2023**, *11*, 15576–15599.

[5] K. Xu, M. S. Ding, S. Zhang, J. L. Allen, T. R. Jow, *J. Electrochem. Soc.* **2002**, *149*, A622.

[6] N. von Aspern, S. Röser, B. Rezaei Rad, P. Murmann, B. Streipert, X. Mönnighoff, S. D. Tillmann, M. Shevchuk, O. Stubbmann-Kazakova, G.-V. Röschenthaler, S. Nowak, M. Winter, I. Cekic-Laskovic, *J. Fluor. Chem.* **2017**, *198*, 24–33.

[7] P. Murmann, N. von Aspern, P. Janssen, N. Kalinovich, M. Shevchuk, G.-V. Röschenthaler, M. Winter, I. Cekic-Laskovic, *J. Electrochem. Soc.* **2018**, *165*, A1935.

[8] C. Liu, Y. Zhao, S. Qiao, K. Zheng, Y. Wang, Z. Sun, T. Liang, C. Fan, T. Zhou, Q. Huang, *Case Stud. Therm. Eng.* **2024**, *58*, 104383.

[9] T. Huang, X. Z. Zheng, G. F. Fang, Y. Pan, W. G. Wang, M. X. Wu, *RSC Adv.* **2017**, *7*, 47775–47780.

[10] T. Huang, X. Zheng, W. Wang, Y. Pan, G. Fang, M. Wu, *Mater. Chem. Phys.* **2017**, *196*, 310–314.

[11] P. Jiang, X. Gu, S. Zhang, J. Sun, S. Wu, Q. Zhao, *Phosphorus Sulfur Silicon Relat. Elem.* **2014**, *189*, 1811–1822.

[12] R. Mishra, M. Anne, S. Das, T. Chavva, M. V. Shelke, V. G. Pol, *Adv. Sustain. Syst.* **n.d.**, *n/a*, 2400273.

[13] A. M. Haregewoin, A. S. Wotango, B. J. Hwang, *Energy Environ. Sci.* **2016**, *9*, 1955–1988.

[14] J. Liu, X. Song, L. Zhou, S. Wang, W. Song, W. Liu, H. Long, L. Zhou, H. Wu, C. Feng, Z. Guo, *Nano Energy* **2018**, *46*, 404–414.

[15] M. Zhou, C. Qin, Z. Liu, L. Feng, X. Su, Y. Chen, L. Xia, Y. Xia, Z. Liu, *Appl. Surf. Sci.* **2017**, *403*, 260–266.

[16] S.-T. Fei, H. R. Allcock, *J. Power Sources* **2010**, *195*, 2082–2088.

[17] K. Xu, *Chem. Rev.* **2004**, *104*, 4303–4417.

[18] T. Dagger, M. Grützke, M. Reichert, J. Haetge, S. Nowak, M. Winter, F. M. Schappacher, *J. Power Sources* **2017**, *372*, 276–285.

[19] T. Dagger, P. Niehoff, C. Lürenbaum, F. M. Schappacher, M. Winter, *Energy Technol.* **2018**, *6*, 2023–2035.

[20] Y. Li, Y. An, Y. Tian, H. Fei, S. Xiong, Y. Qian, J. Feng, *J. Electrochem. Soc.* **2019**, *166*, A2736.

[21] H. W. Rollins, M. K. Harrup, E. J. Dufek, D. K. Jamison, S. V. Sazhin, K. L. Gering, D. L. Daubaras, *J. Power Sources* **2014**, *263*, 66–74.

[22] J. Feng, Y. An, L. Ci, S. Xiong, *J. Mater. Chem. A* **2015**, *3*, 14539–14544.

[23] V. Nilsson, S. Liu, C. Battaglia, R.-S. Kühnel, *Electrochimica Acta* **2022**, *427*, 140867.

[24] S. Liu, M. Becker, Y. Huang-Joos, H. Lai, G. Homann, R. Grissa, K. Egorov, F. Fu, C. Battaglia, R.-S. Kühnel, *Batter. Supercaps* **2023**, *6*, e202300220.

[25] A. Ghaur, C. Peschel, I. Dienwiebel, L. Haneke, L. Du, L. Profanter, A. Gomez-Martin, M. Winter, S. Nowak, T. Placke, *Adv. Energy Mater.* **2023**, *13*, 2203503.

[26] B. A. Sadeghi, C. Wölke, F. Pfeiffer, M. Baghernejad, M. Winter, I. Cekic-Laskovic, *J. Power Sources* **2023**, *557*, 232570.

[27] R. P. Benedetti, *Flammable and Combustible Liquids Code Handbook*, **1987**.

[28] L. Xia, Y. Xia, Z. Liu, *J. Power Sources* **2015**, *278*, 190–196.

[29] A. Yusuf, V. Sai Avvaru, J. De la Vega, M. Zhang, J. Garcia Molleja, D.-Y. Wang, *Chem. Eng. J.* **2023**, *455*, 140678.

[30] S. Sayah, M. Baazizi, M. Karbak, J. Jacquemin, F. Ghamouss, *Energy Technol.* **2023**, *11*, 2201446.

[31] F. Gao, H. Liu, K. Yang, C. Zeng, S. Wang, M. Fan, H. Wang, *Int. J. Electrochem. Sci.* **2020**, *15*, 1391–1411.
[32] K. Matsumoto, K. Nakahara, K. Inoue, S. Iwasa, K. Nakano, S. Kaneko, H. Ishikawa, K. Utsugi, R. Yuge, *J. Electrochem. Soc.* **2014**, *161*, A831–A834.
[33] C. Liao, L. Han, W. Wang, W. Li, X. Mu, Y. Kan, J. Zhu, Z. Gui, X. He, L. Song, Y. Hu, *Adv. Funct. Mater.* **2023**, *33*, 2212605.
[34] R. Gond, W. van Ekeren, R. Mogensen, A. J. Naylor, R. Younesi, *Mater. Horiz.* **2021**, *8*, 2913–2928.
[35] G. A. Giffin, *Nat. Commun.* **2022**, *13*, 5250.
[36] X. Li, W. Li, L. Chen, Y. Lu, Y. Su, L. Bao, J. Wang, R. Chen, S. Chen, F. Wu, *J. Power Sources* **2018**, *378*, 707–716.
[37] G. G. Eshetu, E. Figgemeier, *ChemSusChem* **2019**, *12*, 2515–2539.
[38] S. Chae, M. Ko, K. Kim, K. Ahn, J. Cho, *Joule* **2017**, *1*, 47–60.
[39] C. Wölke, B. A. Sadeghi, G. G. Eshetu, E. Figgemeier, M. Winter, I. Cekic-Laskovic, *Adv. Mater. Interfaces* **2022**, *9*, DOI 10.1002/admi.202101898.
[40] V. Meunier, M. Leal De Souza, M. Morcrette, A. Grimaud, *Joule* **2023**, *7*, 42–56.
[41] P. Yan, M. Shevchuk, C. Wölke, F. Pfeiffer, D. Berghus, M. Baghernejad, G.-V. Röschenthaler, M. Winter, I. Cekic-Laskovic, *Small Struct.* **2024**, *5*, 2300425.
[42] R. D. Deshpande, P. Ridgway, Y. Fu, W. Zhang, J. Cai, V. Battaglia, *J. Electrochem. Soc.* **2014**, *162*, A330.
[43] J. Asenbauer, T. Eisenmann, M. Kuenzel, A. Kazzazi, Z. Chen, D. Bresser, *Sustain. Energy Fuels* **2020**, *4*, 5387–5416.
[44] S. E. Sloop, J. B. Kerr, K. Kinoshita, *J. Power Sources* **2003**, *119–121*, 330–337.
[45] T. Sasaki, T. Abe, Y. Iriyama, M. Inaba, Z. Ogumi, *J. Power Sources* **2005**, *150*, 208–215.
[46] C. Schultz, S. Vedder, B. Streipert, M. Winter, S. Nowak, *RSC Adv.* **2017**, *7*, 27853–27862.
[47] Y. Liao, H. Zhang, Y. Peng, Y. Hu, J. Liang, Z. Gong, Y. Wei, Y. Yang, *Adv. Energy Mater.* **2024**, *14*, 2304295.
[48] S. Wiemers-Meyer, M. Winter, S. Nowak, *Phys. Chem. Chem. Phys.* **2016**, *18*, 26595–26601.
[49] G. Gachot, P. Ribière, D. Mathiron, S. Grugeon, M. Armand, J.-B. Leriche, S. Pilard, S. Laruelle, *Anal. Chem.* **2011**, *83*, 478–485.
[50] A. Ghaur, F. Pfeiffer, D. Diddens, C. Peschel, I. Dienwiebel, L. Du, L. Profanter, M. Weiling, M. Winter, T. Placke, S. Nowak, M. Baghernejad, *Small* **2023**, *19*, 2302486.
[51] D. R. Gallus, R. Wagner, S. Wiemers-Meyer, M. Winter, I. Cekic-Laskovic, *Electrochimica Acta* **2015**, *184*, 410–416.
[52] M. Winter, *Z. Für Phys. Chem.* **2009**, *223*, 1395–1406.
[53] B. Zhang, L. Wang, Y. Zhang, X. Wang, Y. Qiao, S.-G. Sun, *J. Chem. Phys.* **2023**, *158*, 054202.
[54] N. Meddings, M. Heinrich, F. Overney, J.-S. Lee, V. Ruiz, E. Napolitano, S. Seitz, G. Hinds, R. Raccichini, M. Gaberšček, J. Park, *J. Power Sources* **2020**, *480*, 228742.
[55] I. A. J. Gordon, S. Grugeon, H. Takenouti, B. Tribollet, M. Armand, C. Davoisne, A. Débart, S. Laruelle, *Electrochimica Acta* **2017**, *223*, 63–73.
[56] M. Steinhauer, S. Risse, N. Wagner, K. A. Friedrich, *Electrochimica Acta* **2017**, *228*, 652–658.
[57] R. Morasch, H. A. Gasteiger, B. Suthar, *J. Electrochem. Soc.* **2023**, *170*, 080522.
[58] R. Morasch, H. A. Gasteiger, B. Suthar, *J. Electrochem. Soc.* View Article Online DOI: 10.1039/D5LF00138B **2024**, *171*, 050548.
[59] A. L. Michan, B. S. Parimalam, M. Leskes, R. N. Kerber, T. Yoon, C. P. Grey, B. L. Lucht, *Chem. Mater.* **2016**, *28*, 8149–8159.
[60] Y. Jin, N. J. H. Kneusels, L. E. Marbella, E. Castillo-Martínez, P. C. M. M. Magusin, R. S. Weatherup, E. Jónsson, T. Liu, S. Paul, C. P. Grey, *J. Am. Chem. Soc.* **2018**, *140*, 9854–9867.
[61] H. Ota, Y. Sakata, A. Inoue, S. Yamaguchi, *J. Electrochem. Soc.* **2004**, *151*, A1659.
[62] S. Grugeon, P. Jankowski, D. Cailleu, C. Forestier, L. Sannier, M. Armand, P. Johansson, S. Laruelle, *J. Power Sources* **2019**, *427*, 77–84.
[63] J. Yang, N. Solomatin, A. Kraytsberg, Y. Ein-Eli, *ChemistrySelect* **2016**, *1*, 572–576.
[64] M. Preuss, F. Bechstedt, *Phys. Rev. B* **2006**, *73*, 155413.
[65] M. Weiling, C. Lechtenfeld, F. Pfeiffer, L. Frankenstein, D. Diddens, J.-F. Wang, S. Nowak, M. Baghernejad, *Adv. Energy Mater.* **2024**, *14*, 2303568.
[66] C. Wölke, D. Diddens, B. Heidrich, M. Winter, I. Cekic-Laskovic, *ChemElectroChem* **2021**, *8*, 972–982.
[67] R. Petibon, C. P. Aiken, N. N. Sinha, J. C. Burns, H. Ye, C. M. VanElzen, G. Jain, S. Trussler, J. R. Dahn, *J. Electrochem. Soc.* **2013**, *160*, A117–A124.
[68] X. Mönnighoff, A. Friesen, B. Konersmann, F. Horsthemke, M. Grützke, M. Winter, S. Nowak, *J. Power Sources* **2017**, *352*, 56–63.

View Article Online
DOI: 10.1039/D5LF00138B

Data availability

The data that support the findings of this study are available on request from the authors.